TOPICAL REVIEW • OPEN ACCESS

Observing field-induced effects in scanning tunneling microscope junction through lifetimes of resonant electrons

IOP Publishing J. Phys.: Condens. Matter 38 (2026) 043001 https://doi.org/10.1088/1361-648X/ae3873

Journal of Physics: Condensed Matter

TOPICAL REVIEW

Observing field-induced effects in scanning tunneling microscope junction through lifetimes of resonant electrons

Wei-Bin Su[1,*], Shin-Ming Lu[1], Horng-Tay Jeng[1,2,*] and Chia-Seng Chang[1]

[1] Institute of Physics, Academia Sinica, Nankang, Taipei 11529, Taiwan
[2] Department of Physics, National Tsing Hua University, Hsinchu 30013, Taiwan
[*] Authors to whom any correspondence should be addressed.

E-mail: wbsu@phys.sinica.edu.tw, jeng@phys.nthu.edu.tw, simonluyang@gmail.com and jasonc@phys.sinica.edu.tw

Keywords: scanning tunneling microscope, field emission resonance, resonant electron lifetimes, quantum trapping, tip-induced attractive deformation, wave function dissipation

OPEN ACCESS

RECEIVED
28 November 2024

REVISED
20 December 2025

ACCEPTED FOR PUBLICATION
14 January 2026

PUBLISHED
30 January 2026

Abstract

Field emission resonance (FER) arises from the coupling of field-emitted electrons from the tip of scanning tunneling microscope (STM) with quantized states formed in the STM junction. The average lifetime of FER electrons, reflected in the linewidth according to the uncertainty principle, has been rarely explored. Here, we review our recent findings on using FER linewidth to probe field-induced effects within STM junction, including quantum trapping occurring on MoS_2 and Ag(100) surfaces, as well as the attractive deformation on graphite surfaces. We demonstrate that the FER linewidth on MoS_2 and Ag(100) surfaces can vary by up to tenfold, which is an outcome of the quantum trapping coupled with mechanisms such as correlated two-electron tunneling through exchange interaction, energy gap above the vacuum level, spin flip, light emission, and the Pauli exclusion principle. This substantial FER linewidth variation is absent on the Ag(111) surface due to the lack of an energy gap above the vacuum level. The finite lifetimes of resonant electrons signify that the FER wave function decays at a rate proportional to the FER linewidth. We find that this decay rate remains nearly unchanged with increasing FER electric field on Ag(111) surface, while it rises with field strength on graphite. This marked difference arises from the more pronounced attractive deformation of graphite, with the deformed top layer resembling monolayer graphene.

1. Introduction

As a strong electric field is applied to a material, electrons are emitted to form a current in the vacuum. This phenomenon is known as field emission [1]. In a typical field emission apparatus, the distance from the material to the ground ranges from millimeter to micrometer, and the emission current monotonically increases with the electric field. Nevertheless, as this distance becomes comparable to that in a junction of scanning tunneling microscope (STM), electron energies in the vacuum gap are quantized. Consequently, the differential emission current oscillates with the bias voltage, a phenomenon known as field emission resonance (FER), first theorized by Gundlach in 1966 [2]. FER was first verified experimentally in metal-oxide-semiconductor tunneling junction [3]. In these early setups, FER could only be observed under varying electric fields due to the fixed oxide layer thickness. This limitation was overcome with the advent of STM [4], where the vacuum gap could be precisely controlled via the feedback mechanism. The first demonstration of FER using STM was achieved by Binnig *et al* and Becker *et al* on Ni(100) and Au(110), respectively [5, 6], through distance–voltage (Z–V) spectroscopy.

Although FER results from the coupling of field emission with quantized states in the STM vacuum junction, it also provides insights into the characteristics of both the tip and surface. As a result, FER has been widely employed as a powerful tool for exploring diverse physical phenomena since FER became observable with STM. For instance, diamond is an insulator that cannot be probed by STM under conventional tunneling conditions. Nevertheless, Bobrov *et al* demonstrated that FER enables imaging of

the diamond surface and even achieves atomic resolution [7]. Liu *et al* demonstrated that FER energies, which usually depend on the set current and tip sharpness, can also be substantially shifted downward by illuminating Ag tips with visible light [8]. Barimar *et al* showed that FER can be applied to investigate silicon-on-insulator devices with varying doping levels, where the nano-scale spreading resistance is estimated from the energy shifts of FER peaks [9]. Wahl *et al* and Pascual *et al* presented that resonant electrons in the lowest-order FER can interact with surface step to form the interference pattern, from which the dispersion relation of resonant electrons is derived [10, 11]. Likewise, Stepanow *et al* and Craes *et al* exhibited that FER electrons can couple with quantum dots, revealing lateral quantization [12, 13]. Furthermore, the energies of FER peaks can serve as an indicators of local work function variations across surfaces, as demonstrated in studies of heteroepitaxial growth [14–16], graphene quantum dots [17], heterostructures with moiré patterns [18], nitrogen-doped graphene [19], and monolayer 2D materials [20–28]. Additionally, the intensities of FER peaks can provide information on the local electron transmissivity of surface with reconstruction, such as Si(111)7 $\times$ 7 [29], Au(111)22 $\times$ $\sqrt{3}$ [30], and FeO/Pt(111) [31]. The appearance of zero intensities at the valleys of an FER peak indicates that a substance possesses a band gap above the vacuum level, as observed for Ag(100) [31]. Moreover, FER peak count can serve as an indicator of the sharpness level of the STM tip [32, 33] and of its field enhancement factor [34]. Besides energy, intensity, and peak number, the FER linewidth represents a physical quantity whose reciprocal gives the average lifetime of FER electrons, as dictated by the uncertainty principle. However, FER linewidth has seldom been used to explore surface phenomena, likely because surface phenomena that lead to substantial linewidth variation have not been discovered yet.

In this topical review, we begin by introducing quantum trapping, a field-induced phenomenon in the STM junction that can cause up to a tenfold change in FER linewidth [35, 36]. Quantum trapping can be described using the square-well model in quantum mechanics, which typically presents two scenarios. In the first, quantum confinement occurs when the particle energy is smaller compared to the well depth, giving rise to discrete energy levels known as quantum-well states. In the second, quantum scattering arises when a particle approaches the square well from outside, having an energy exceeding the well depth. Because particles exhibit wave-like behavior, only those with specific energies can transmit completely through the square well, which is known as resonance transmission. Previous studies have shown the presence of quantum-well states and resonance transmission on Pb [37, 38] and Ag films [39, 40], respectively, due to their free-electron-like electronic structures.

Quantum trapping is entirely different from quantum confinement and scattering, in that the particle already resides within the well while possessing energy exceeding the square-well depth. Due to its wave nature, the particle can be transiently captured within the well but ultimately escapes since its energy is greater than the well depth. The mean duration the particle remains trapped oscillates with the well size. It is found that the FER linewidth observed on bulk MoS_2 and Ag(100) surfaces exhibits substantial variation [35, 36], which is a reflection of the quantum trapping. We suggest that mechanisms and processes through which quantum trapping information influences the linewidth include the presence of an energy gap above the vacuum level, correlated two-electron tunneling via exchange interaction, spin flip, light emission, and Pauli exclusion principle. Significant linewidth variation indicates fluctuations in the dissipation rate of the quantized state's wave function in FER [36]. Interestingly, this pronounced linewidth variation is absent on the Ag(111) surface, resulting from a nearly constant dissipation rate of wave function.

Secondly, we present the use of FER linewidth to detect field-induced attractive deformation on the graphite surface. Under typical conditions, the electric field between the tip and surface ranges from 0.1 to 0.3 V $Å^{-1}$, which is strong enough to modify the structural and electronic properties of the surface. For instance, the quantum well state, surface state, and resonance transmission can be perturbed by the electric field, inducing displacements in their energy levels [41–43]. Additionally, this field can locally induce expansion in Pb films due to electrostatic forces, an effect known as attractive deformation [44]. This deformation is even more pronounced for the suspended graphene [45, 46]. Therefore, an attractive deformation is expected on the graphite surface and is likely more significant than on the metallic Ag(111) surface, owing to the considerably weaker interlayer van der Waals force compared to metallic bonding. We find that this difference in attractive deformation can be detected through measuring the electric field and FER linewidth to determine the dissipation rate of wave function [47].

The electric potential within the STM junction is commonly considered to be linear, suggesting that the tip resembles a flat plate. However, in practice, the tip apex is generally regarded as composing a base having a characteristic radius of several hundreds of angstroms, surmounted by a small protrusion. Whenever this protrusion is terminated by a single atom, STM is capable of achieving atomic resolution. Under such a tip structure, the electric field within STM junction is non-uniform and cannot simply be

approximated as the applied voltage divided by the distance from the surface to the tip. However, accurately measuring the FER electric field, which is affected by tip sharpness, is essential to reliably determine the dissipation rate of wave function. Furthermore, apart from the electric field, quantum trapping is also sensitive to the base radius of the tip. Thus, characterizing both the sharpness and the base radius of an STM tip is crucial for fully understanding field-induced quantum trapping and attractive deformation, which can be addressed using FER energies [48]. Next, let us introduce this method.

2. Characterizing STM tip apex structures based on FER energies

The schematic in figure 1(a) depicts the STM tip apex as a cone (indicated by an arrow) mounted on a base having a curvature radius R. The opening angle θ of the cone determines the tip sharpness, with smaller angles corresponding to sharper tips. In principle, a shaper tip enhances field inhomogeneity; specifically, while the electric field for field emission near the tip apex is strengthened, the field near the surface for FER is reduced due to the conservation of electric potential. Moreover, a sharper tip can emit a higher field emission current because the width of the tunneling energy barrier is reduced [33]. Thus, in the Z–V spectroscopy, maintaining a constant current requires a greater tip-surface distance for a sharper tip. A longer distance allows for the accommodation of more quantized states for FER. As a result, more FER peaks can be observed when a tip with higher sharpness is used.

Four FER spectra shown in figure 1(b) were recorded at the same current on Ag(111). The number N, indicated on the right, represents FER peak count, which ranges from 7 to 22 depending on the tip sharpness. The zeroth-order peak in figure 1(b), labeled 0, reflects the formation of a quantized state in the electric potential produced by the overlap of the applied and image potentials. For FER peaks of order greater than zero, the relevant potential is solely the applied potential. If the applied potential is linear, the peak energy E_n of order n greater than 0 can be described by the triangular potential model:

$$E_n = E_{vac} + \alpha F_{FER}^{\frac{2}{3}} \left(n - \frac{1}{4} \right)^{\frac{2}{3}}, \tag{1}$$

where E_{vac} is the vacuum level, F_{FER} is the field for forming FER, and

$$\alpha = \left(\frac{\hbar^2}{2m} \right)^{\frac{1}{3}} \left(\frac{3\pi e}{2} \right)^{\frac{2}{3}}. \tag{2}$$

In other words, equation (1) can be used to assess whether the applied potential in STM junction is non-linear. The graph in figure 1(c) presents E_n as a function of $(n - 1/4)^{2/3}$ for FER spectra displayed in figure 1(b). This graph shows that the markers for $n = 1$–3 align along a straight line, while those for n greater than 3 exhibit a clear deviation from the linearity, with the discrepancy becoming more pronounced as n increases. This result indicates that F_{FER} remains consistent for $n = 1$, 2, 3, but weakens with n for $n > 3$. To explain this weakening of F_{FER}, we consider the case where the base is perfectly flat ($R = \infty$). Based on electrostatics principle, the electric field along the surface normal remains uniform, with field enhancement occurring only in the vicinity of the protrusion [49]. Therefore, the peak energies at every order conform to equation (1) for a planar base. In practice, however, the base is not perfectly planar, the field responsible for FER formation is no longer uniform and is weaker than in the planar scenario. Consequently, equation (1) fails to account for the FER energies across all orders when the base is curved. Therefore, the deviation from the linear fit arises due to the base curvature. The reduction in the electric field strength caused by the curved base becomes more pronounced with increasing the tip-surface distance. As a result, with increasing n, which reflects a greater tip–surface separation, the FER energy departs more strongly from equation (1), leading to the downward-curved profiles evident in figure 1(c).

For the values corresponding to $n = 1$–3 at smaller tip-surface separations, the planar base serves as a reasonable approximation, allowing these values to be fitted with a line of slope S_1, given by $\alpha F_{FER}{}^{2/3}$. Thus, F_{FER} of these three orders can be determined from the graph of E_n as a function of $(n - 1/4)^{2/3}$. As shown in figure 1(c), S_1 rises with decreasing N, enabling sharpness representable by $1/S_1$. Moreover, since F_{FER} diminishes with increasing sharpness, as demonstrated by the FER peak of the first order labeled 1 in figure 1(b), higher-order FER peaks shifts to a lower energy with increasing N.

Figure 1(d) shows that FER energies of $n = 4$–6 at $N = 7$ fit a line with slope S_2, a trend that is also observed for other N. Because of the curvature of the base, the slope S_2 is lower than S_1. Therefore, the ratio S_2/S_1 serve as an indicator of the base radius, with $S_2/S_1 = 1$ in the planar case. For acquiring FER

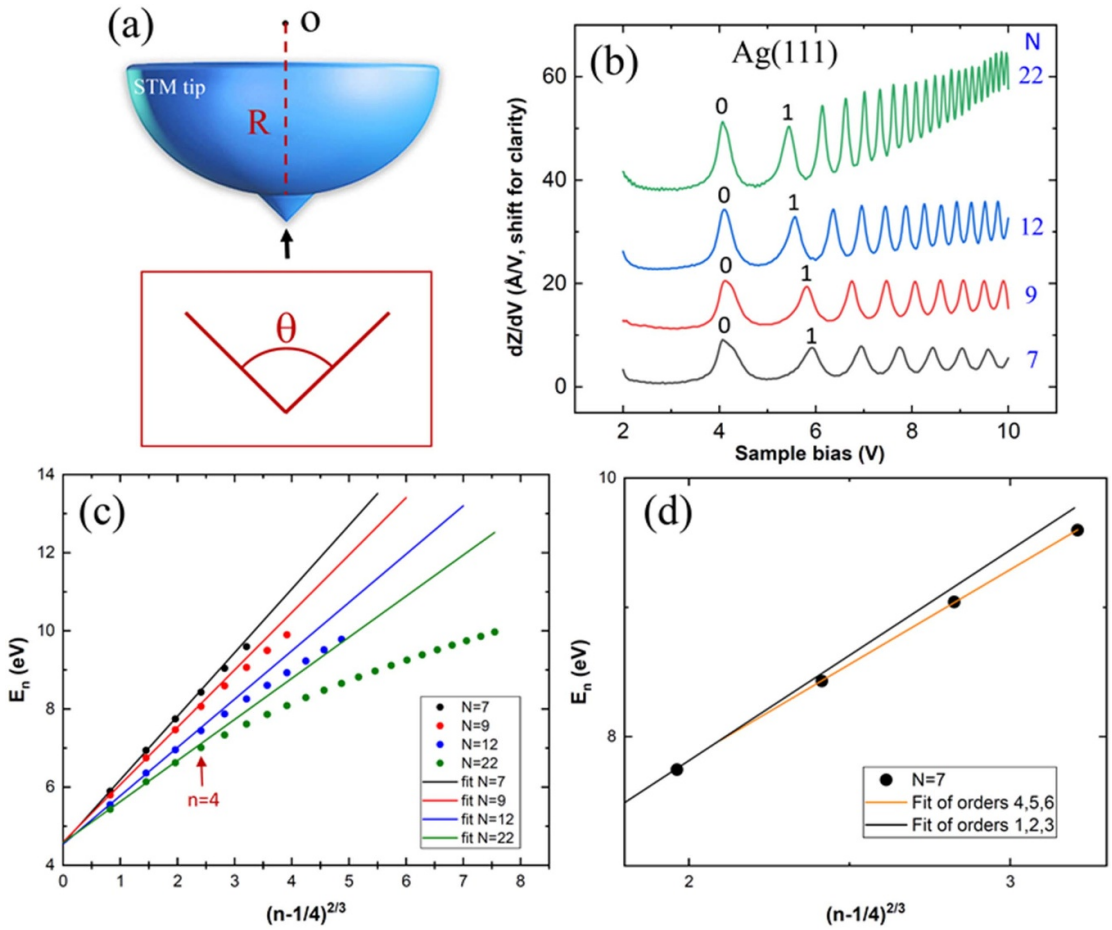

Figure 1. (a) Schematic of the STM tip apex, featuring a base characterized by a radius R and a cone-shaped protrusion. The opening angle θ quantifies the sharpness. (b) Four differential dZ/dV-V spectra measured on the Ag(111), displaying varying FER peak numbers. The numerals indicate the first as well as zeroth order peaks, while N specifies the total peak count. (c) Graph of E_n as a function of $(n - 1/4)^{2/3}$ for peaks of orders n $\geqslant$ 1 from (b), showing for all N, downward-curved trends beginning at $n = 4$. (d) Linear fit of fourth-, fifth, and sixth-order values at $N = 7$. Reproduced from [48].© 2022 The Japan Society of Applied Physics. All rights reserved.

spectra, the bias is typically ramped up to 10 V, which can alter the tip sharpness. Furthermore, continuous Z–V spectroscopy may gradually degrade the protrusion, leading to the loss of FER. Whenever this occurs, tip sharpness is restored using voltage pulses, or we replace the tip. Consequently, FER spectra containing various numbers of peaks are collected.

Figure 2(a) plots S_2/S_1 versus $1/S_1$ for spectra acquired on Ag(111), showing distinct flat regions highlighted with dashed horizontal lines. These plateaus indicate that the sharpness varies while the base remains constant, probably resulting from the repetitive measurement of FER spectra. Moreover, the separate plateaus suggest that the base size may be significantly different, ascribed to applying voltage pulses or substituting tips. The graph also shows that the base radii can be different while the sharpness is identical, as evidenced by the measurements positioned on a dashed vertical line in figure 2(a). Two spectra associated with S_2/S_1 values of 0.85 and 0.8 on this dashed line are shown in figure 2(b). The energies are nearly identical for the peaks of $n = 1$–4, indicating consistent sharpness. However, the energies differ for the peaks of $n = 5$–7, reflecting variations in base radii, with the energy difference increasing as n increases [see figure 2(c)]. This finding suggests that a greater base enhances field strength.

Figure 1(b) illustrates that, for peaks of the same order, the FER linewidth decreases with increasing FER number. However, this trend does not hold for the MoS_2 and Ag(100) surfaces.

3. Quantum trapping observed on MoS_2 and Ag(100) surfaces

Figure 3(a) presents a differential Z–V spectrum obtained from a bulk MoS_2 surface (inset), revealing five FER peaks. A dashed line in figure 3(a) represents zero intensity. Valleys surrounding the second-order FER (FER2) peak, as indicated by arrows, drop to zero, suggesting that a bulk MoS_2 exhibits

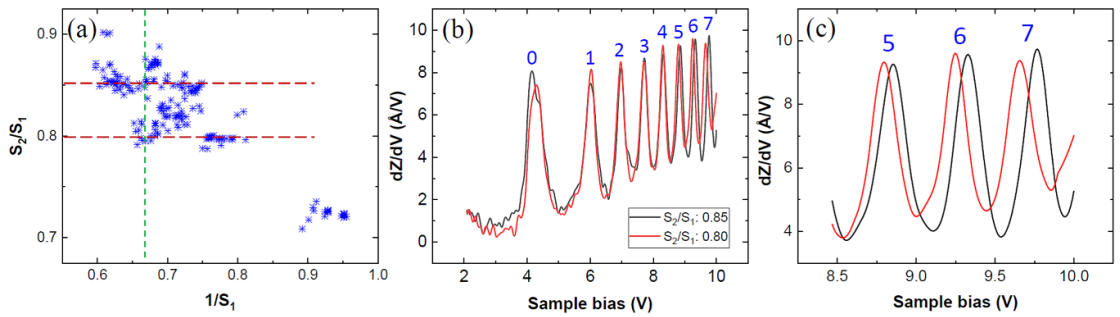

Figure 2. (a) Graph of S_2/S_1 versus $1/S_1$ from collected spectra, highlighting flat regions (dashed horizontal lines). A dashed vertical line indicates values obtained from tips having different radii of the base but the same sharpness. (b) Two dZ/dV-V spectra associated with two values on the dashed vertical line in (a). (c) Peaks of $n = 5$–7 from (b), presenting an energy shift for the same n, which becomes pronounced as n increases. Reproduced from [48]. © 2022 The Japan Society of Applied Physics. All rights reserved.

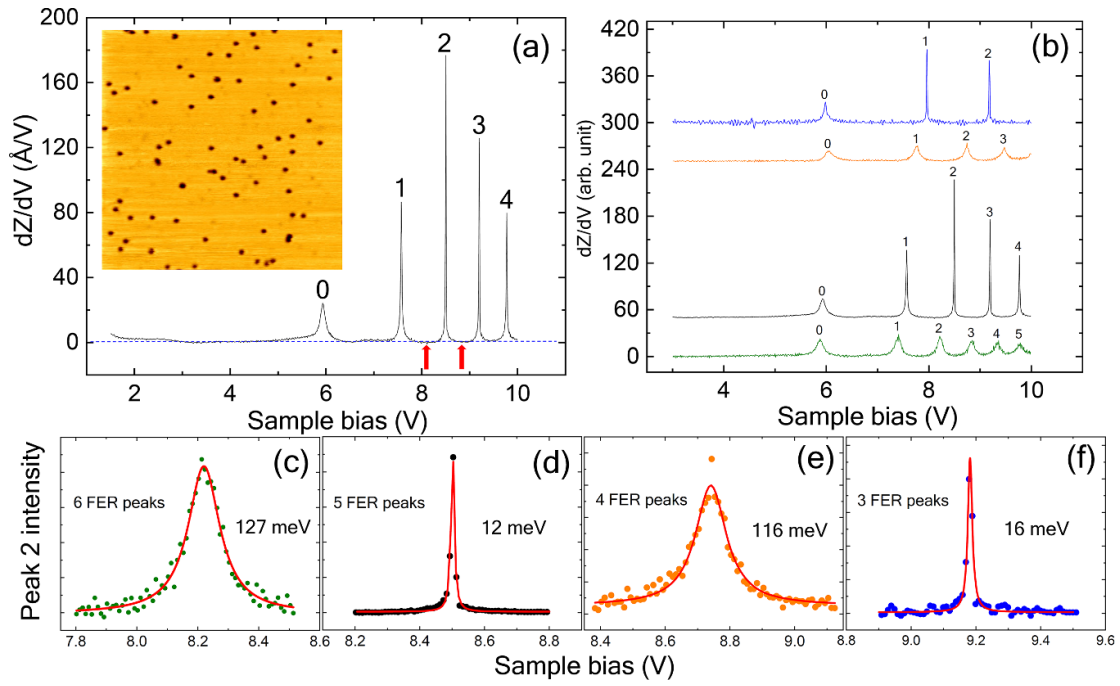

Figure 3. (a) dZ/dV-V spectrum showing five peaks. The dashed line represents that the spectral intensity is zero, highlighting that the valley intensities (indicated by arrows) surrounding the FER2 peak reach 0. Inset: the representative topography image on the surface of bulk MoS_2, measuring 100 × 100 nm^2. (b) FER spectra displaying three, four, five, and six peaks. (c)–(f) Lorentzian fit of the FER2 peaks from (b), showing that the extracted linewidths vary depending on the number of FER peaks. Reproduced with permission from [35]. CC BY 3.0.

an energy gap above the vacuum level and that the FER2 peak falls within this gap [31]. Figure 3(b) presents FER spectra containing three, four, five, and six peaks. FER peaks of orders higher than zero in the three- and five-peak spectra are considerably narrower than those in the four- and six-peak spectra. This behavior contrasts sharply with that seen on Ag(111) surface (figure 1(b)). Given the zero intensity in the valleys, the FER2 peak provides an ideal feature for linewidth analysis. Figures 3(c)–(f) depict Lorentzian fit for FER2 peaks in figure 3(b). The extracted linewidths oscillate with the number of FER peaks, differing by up to a factor of ten. Notably, the linewidth can be down to 12 meV in the five-peak spectrum, a result not previously observed.

Ag(111) is a metal with no energy gap above the vacuum level, whereas dielectric bulk MoS_2 has such a gap. Therefore, the variation in linewidth with the number of FER peaks, as shown in figure 3, may result from either the dielectric property or the presence of an energy gap. Since Ag(100) exhibits a band gap above the vacuum level, as shown in figure 4, it serves as an ideal system to verify whether the energy gap plays a role in the substantial linewidth variation. Accordingly, we compare the FER linewidths on Ag(100) and Ag(111).

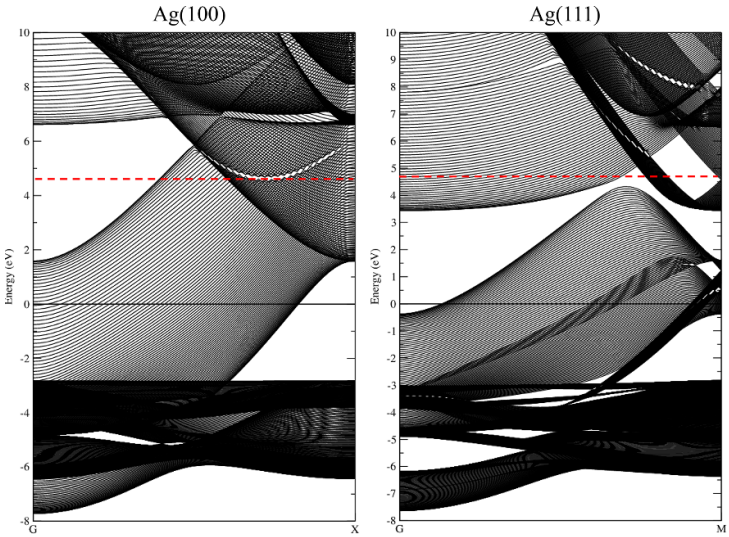

Figure 4. Projected band structures for the Ag(111) (right) and Ag(100) (left). The dashed lines represent the vacuum levels of both surfaces. The Ag(100) surface exhibits an band gap above the vacuum level, while the Ag(111) surface shows no such gap. Reprinted (figure) with permission from [36], Copyright (2022) by the American Physical Society.

Figures 5(a) and (b) show representative FER spectra obtain from Ag(111) and Ag(100), respectively. Figure 5(c) plots the FER energies of higher-order peaks from figures 5(a) and (b) against $(n - 1/4)^{2/3}$. The values for both spectra align closely with linear fits for orders $1 - 3$ but deviate noticeably beyond order 3, similar to the case in figure 1(c). Figure 5(c) shows parallel lines, signifying that the F_{FER} required to form first- through third-order peaks is identical in these two spectra. In figure 5(b), the horizontal dashed line marks that the zero intensity, with the valleys around the first-order FER (FER1) peak (indicated by upward arrows) reaching zero intensity. This result reflects the presence of a band gap in Ag(100) and suggests that the FER1 peak energy lies within this gap. In contrast, the zero valley intensity is absent in figure 5(a) because Ag(111) lacks an energy gap. Thus, FER1 can be used to examine whether the energy gap influences the FER linewidth. Figures 5(d) and (e) show the FER1 peaks from figures 5(a) and (b), in that order. Despite being measured at the identical F_{FER}, the FER1 was prominently narrower on Ag(100) compared to that on Ag(111), evidenced by respective linewidth ΔE values. This difference indicates that the lifetimes of FER electrons on Ag(100) and Ag(111) may vary significantly.

We collected FER spectra with varying tip sharpness levels on Ag(100) as well as Ag(111) surfaces to observe ΔE under different F_{FER} conditions for each surface. Figure 6(a) shows a plot of $1/\Delta E$ against F_{FER}, indicating that the measurements for Ag(100) are notably higher than those for Ag(111) over a specific F_{FER} interval. This finding reveals that the lifetimes of FER1 electrons on Ag(100) is longer than on Ag(111). Additionally, the fluctuation in $1/\Delta E$ is considerably larger for Ag(100) than for Ag(111). Therefore, substantial variation in FER linewidth can also occur on the Ag(100) surface, suggesting that the linewidth is influenced by the presence of an energy gap rather than by dielectric properties. We propose that the pronounced linewidth fluctuations on MoS_2 and Ag(100) surface are attributable to FER detecting quantum trapping.

3.1. Quantum trapping

The square-well model in quantum mechanics provides a basis for understanding quantum trapping, where a particle resides in the square well despite having energy exceeding its depth (figure 7(a)). Within the well, the particle undergoes oscillatory motion because standing waves form. Nevertheless, these standing waves gradually diminish over time, as outside the well, the wave function consists of traveling waves rather than evanescent waves. Consequently, the particle ultimately escapes from the well. Calculations indicate that the average duration the particle remains trapped varies periodically with the well size (figure 7(b)). The maxima of duration are referred to as resonance trapping [35]. Quantum trapping can occur because there exists a surface potential well beneath the STM tip.

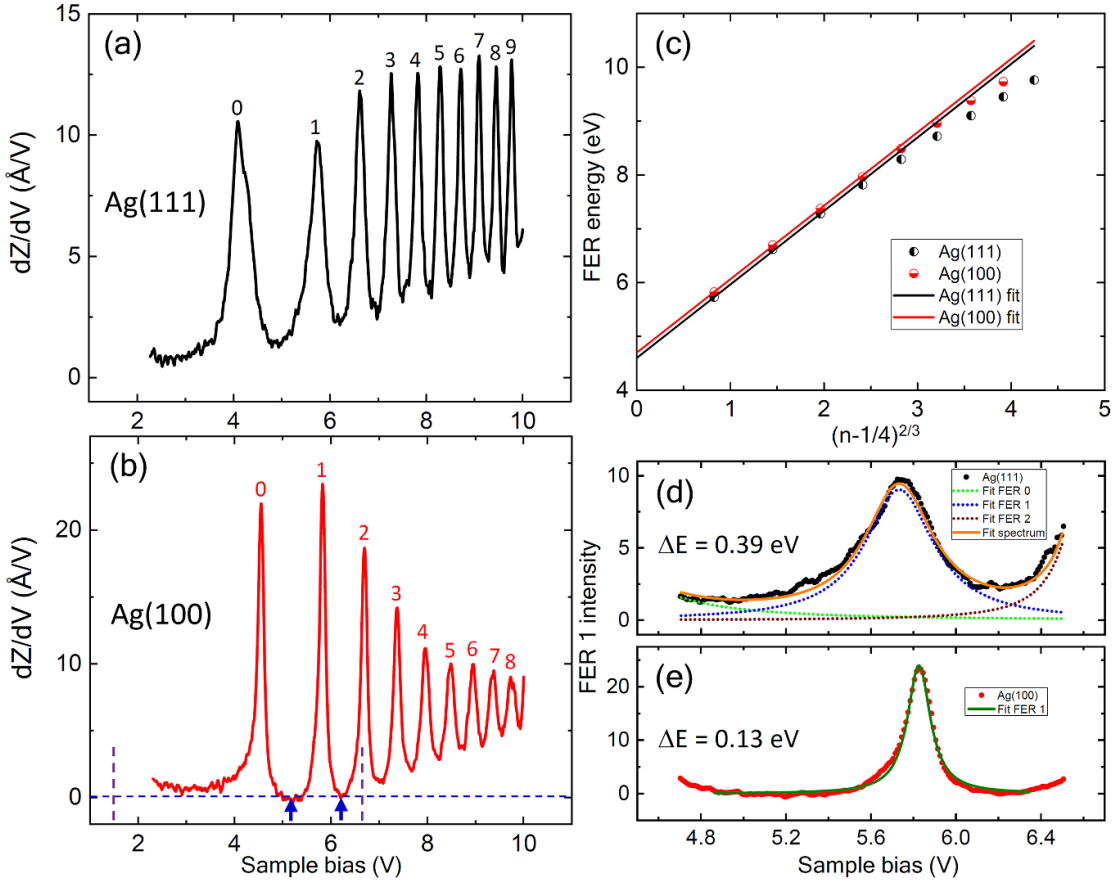

Figure 5. Representative spectra recorded on (a) Ag(111) and (b) Ag(100) surfaces. In (b), the dashed horizontal line denotes that the spectral intensity is zero. The intensities at valleys (indicated by two arrows) surrounding the FER1 peak are precisely zero, confirming the presence of an energy gap in Ag(100), with the FER1 energy lying within this gap. The gap range, determined from the Ag(100) band structure displayed in figure 4, is indicated by vertical dashed lines. (c) Higher-order peak energies in (a) and (b) plotted against $(n-1/4)^{2/3}$. (d) ΔE of FER1 peak in (a), determined through Lorentzian fit and separation of intensity contributions from overlapping FER0 and FER2 peaks. (e) ΔE of the FER1 peak in (b), directly determined via Lorentzian fitting because the valley intensity is zero. Reprinted (figure) with permission from [36], Copyright (2022) by the American Physical Society.

3.2. Field-induced surface potential well formed under the STM tip

3.2.1. Local potential well arising from the surface dipole layer (SDL) on Ag(100)

Figure 8(a) illustrates that despite a tip geometry comprising a nanometer-scale base and an atomically sharp protrusion, the potential remains uniform on the Ag surface, according to the electrostatics principle. Thus, a potential well is unlikely to form directly beneath the tip. However, involving the surface dipole layer (SDL) permits the emergence of a potential well. The SDL arises from electrons spilling into the vacuum, producing a negatively charged layer above and a positively charged layer below the surface [50], as depicted in figure 8(b). Based on electrostatics principles, a flat base sustains a spatially uniform surface electric field [48]. We posit that this uniform field is intense enough to inhibit electron spillover (figure 8(c)). In the case of a curved base, a localized domain of a constant field persists under the protrusion. Beyond this domain, the field strength diminishes progressively away from the center. As a result, the local electron density (as indicated by the scale bar) and its spatial extent beyond the uniform-field domain steadily rise from zero toward their asymptotic field-free values. This redistribution of charge gives rise to a confining potential well for surface electrons, as illustrated in figure 8(d). Figure 8(e) further exhibits that the potential well size is reduced as the identical protrusion is mounted on a smaller base than in figure 8(d).

3.2.2. Local potential well due to polarization charge on MoS_2 surface

MoS_2, a dielectric material having a relative permittivity of 3.7 [51], allows its surface to be penetrated by the external electric field, generating a positive surface polarization charge and inducing band bending within the material [52]. A surface electron situated beneath the STM tip experiences electrostatic repulsion from the applied vacuum field (figure 9(a)) and attraction to the polarization charge. As a result, the resultant surface electric potential arises from the applied potential as well as the potential generated

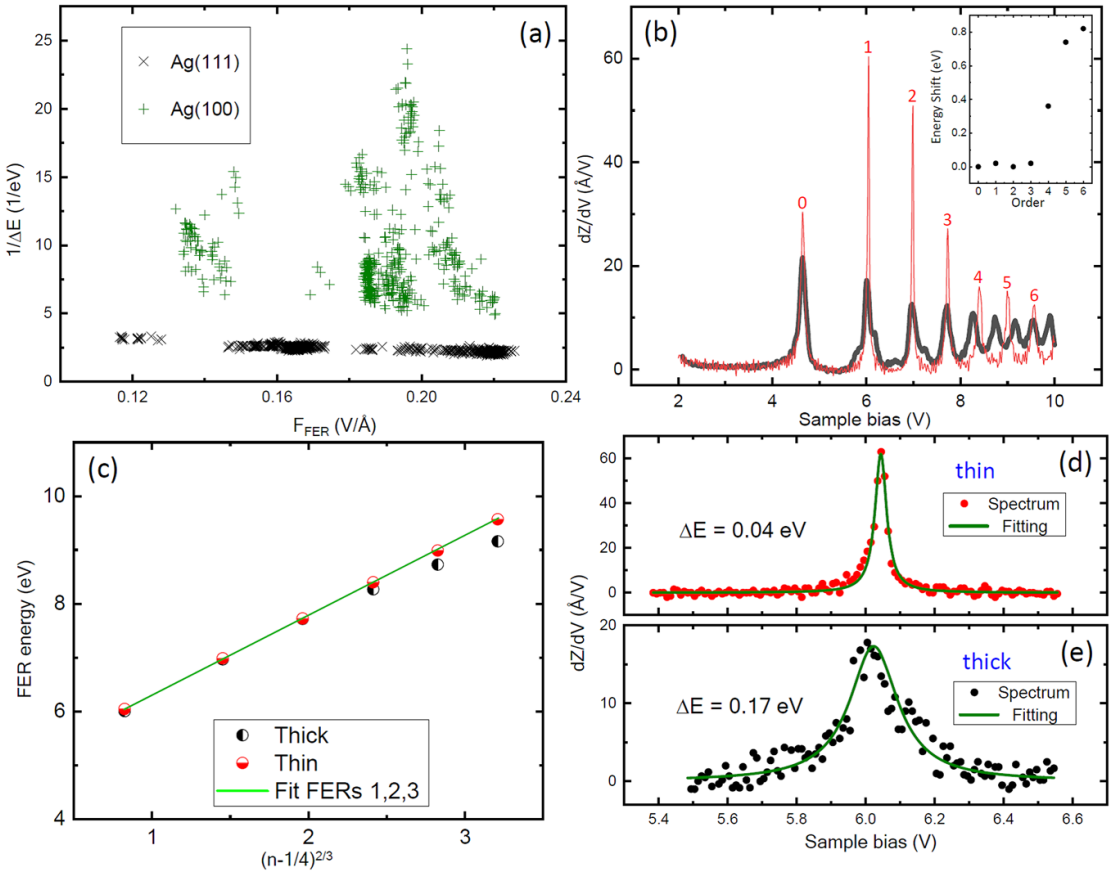

Figure 6. (a) Graphs of $1/\Delta E$ plotted against F_{FER} for Ag(100) and Ag(111). (b) Two spectra (thick and thin) recorded on Ag(100) surface. Inset: energy shift between the same-order peaks against the order. (c) FER energy as a function of $(n-1/4)^{2/3}$ for these two spectra, with a linear fit shown for the FER1, FER2, and FER3 data points. (d) FER1 peak in the thin spectrum, with a fitted linewidth of $\Delta E = 0.04$ eV. (e) FER1 peak in the thick spectrum, with a fitted linewidth of $\Delta E = 0.17$ eV. Reprinted (figure) with permission from [36], Copyright (2022) by the American Physical Society.

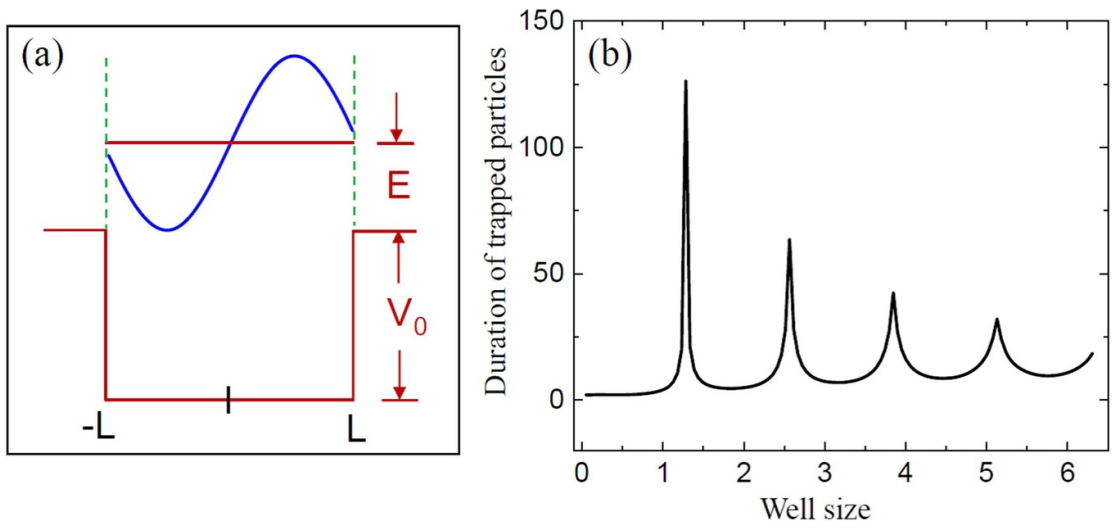

Figure 7. (a) Schematic of a square well having a 2 L width, used to model quantum trapping. In this model, the particle trapped in the well has energy E exceeding the well's depth V_0, with a wave function forming a standing wave. (b) Variation in trapping duration oscillating with the well size. Reproduced with permission from [35]. CC BY 3.0.

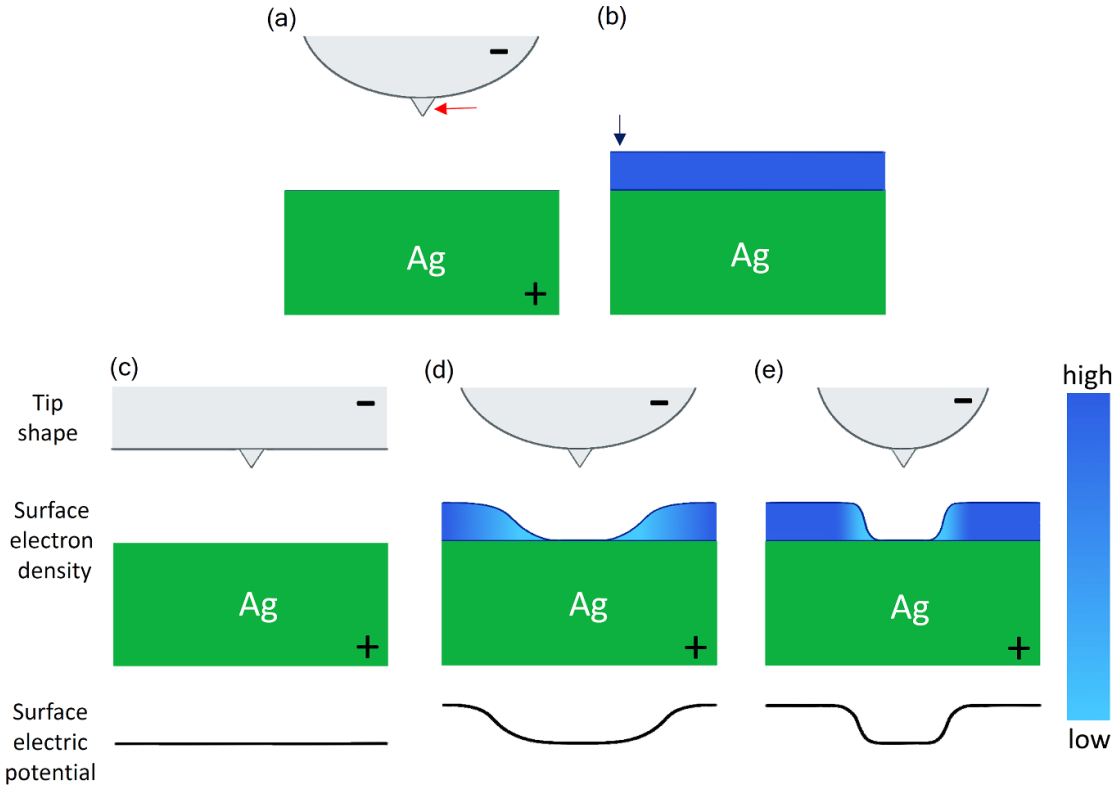

Figure 8. (a) The electrostatic potential is maintained uniform on the Ag surface, despite the tip apex comprises of a curved base topped by a conical protrusion. (b) Negatively charged layer develops above the surface because of electron spillover into the vacuum. (c) Assuming the base is planar and the electric field is sufficiently strong to prevent electron spillover. (d) For a curved base, a confining potential well for surface electrons emerges beneath the tip on Ag surface. (e) The potential well size is reduced as the identical protrusion is placed on a smaller base than in (d). Reprinted (figure) with permission from [36], Copyright (2022) by the American Physical Society.

by the polarization charge. Figure 9(b) plots the higher-order peak energies from figure 3(b) against $(n–1/4)^{2/3}$. Again, for cases involving four, five, and six FER peaks, the data points align well with linear fits. From these slopes and the extrapolated intercepts, the F_{FER} and E_{vac} of each spectrum can be determined. The F_{FER} acquired from figure 9(b) is located at the dashed line shown in figure 9(a), which is perpendicular to the surface as well as ranges from the turning point (denoted by a cross) of the resonant electron to the surface (denoted *o*).

Figure 9(c) shows the projected bulk bands of MoS_2, obtained from density functional theory (DFT) calculations [53–57], spanning energies from 1 to 12 eV higher than the Fermi level. An energy gap is identified above the vacuum level of 5.2 eV [58], where the Γ point band edges lie at 6.1 eV and 8.2 eV, respectively (indicated by lines 2 and 3). This band gap accounts for the zero intensity observed in figure 3(a). Nonetheless, the FER2 energy of 8.5 eV in figure 3(a) lies beyond the calculated energy gap, as denoted by the dashed line in figure 9(c). Band bending accounts for this apparent discrepancy. From figure 9(b), the extrapolated vacuum level E_{vac} is 6.45 eV for the spectrum containing five FER peaks, giving a band-bending potential V_{b} of 1.25 eV (6.45–5.2). Figure 9(c) shows, on the right, how band bending causes the vacuum level (line 1) and the band edges to shift upward near the surface. Consequently, on the surface, the band edges lie at 7.35 eV and 9.45 eV, placing FER2 within the band gap and reconciling the experimental observation.

Normal to the surface, the applied potential takes the form $V_{\mathrm{b}} + F_{\mathrm{FER}}\, z$, where z corresponds to the height above the surface. Under the turning point, the applied potential U_{L} is given by [10]

$$U_{\mathrm{L}}(\rho, z) = \frac{(V_{\mathrm{b}} + F_{\mathrm{FER}} z)}{\left[1 + \left(\frac{\rho}{\rho_0}\right)^2\right]}, \tag{3}$$

where ρ represents the horizontal distance from the dashed line and ρ_0 is a constant, following the distribution curve in figure 9(a). From equation (3), the surface electric field $F_{\mathrm{s}}(\rho)$ is expressed as F_{FER}

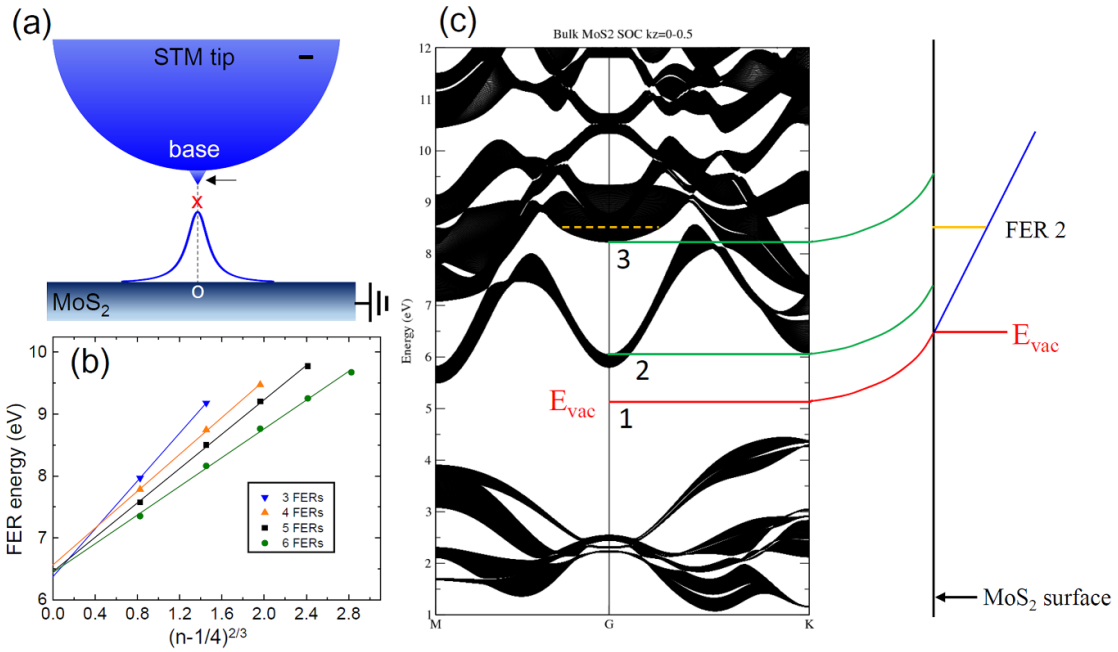

Figure 9. (a) The electric field associated with FER peaks lies along the dashed line perpendicular to the surface, which is between the turning point (cross) and the origin (o). Below the turning point, the electric potential exhibits a distribution curve owing to tip structure. (b) The higher-order FER energies from figure 3(b) plotted against $(n\text{-}1/4)^{2/3}$, revealing a linear trend. Using the slope and intercept, the electric fields and the vacuum levels corresponding to spectra with different numbers of FER peaks are determined. (c) MoS_2 projected bulk bands acquired from DFT calculation, spanning energies 1–12 eV higher than the Fermi level. Line 1 marks the vacuum level, and lines 2 and 3 indicate Γ point band edges. The right-hand energy diagram illustrates the upward shift of both the vacuum level and band edges near the surface, caused by band bending. Reproduced with permission from [35]. CC BY 3.0.

$/[1+(\rho/\rho_0)^2]$. The corresponding polarization charge density $\sigma(\rho)$ is then given by

$$\sigma(\rho) = \frac{\varepsilon_0(\varepsilon_r - 1)F_s}{\varepsilon_r}, \tag{4}$$

where ε_r is the MoS_2 dielectric constant. The resultant potential U_r on the surface is the superposition of the potential $U_P(\rho)$ resulting from the polarization charge and $U_L(\rho,0)$. As ρ approaches infinity, both U_P and U_L vanish. Thus, the sign of U_r at the origin determines whether a surface electron experiences a potential well, namely $U_p(0)+ U_L(0,0)$. Here, $U_L(0,0)$ corresponds to V_b, the band-bending potential, while $U_p(0)$ is given by

$$U_p(0) = -\int_0^\infty \frac{\sigma(\rho)\,2\pi\,\rho \mathrm{d}\rho}{4\pi\,\varepsilon_0\rho}, \tag{5}$$

with ρ_0 being the sole parameter for determining U_r. In figure 10, U_r is plotted as a function of ρ_0 for three electric fields derived from figure 9(b), showing that once ρ_0 exceeds 18 Å, U_r becomes negative. Since ρ_0 is linked to the effective radius of the tip base, which is typically on the order of the hundreds of angstroms, it is reasonable to take ρ_0 to exceed 18 Å. Consequently, the negative U_r reveals the presence of a surface potential well under the tip. Furthermore, for a fixed ρ_0, U_r decreases as F_{FER} increases, implying that the potential well deepens with stronger F_{FER}.

Since FER electrons move back and forth perpendicular to the surface between the turning point and the surface, FER electrons can remain unaffected by the potential well. However, as excited electrons, FER electrons can relax by emitting light [59, 60], transitioning into relaxed electrons that acquire transverse kinetic energy from the inhomogeneous field within the STM junction. As a result, relaxed electrons can experience quantum trapping. Information about the quantum trapping is then transmitted to the FER electrons through the following mechanisms.

3.3. Mechanisms for transmitting quantum trapping information

3.3.1. Correlated two-electron tunneling in FER via exchange interaction

The strongest electric field is at the conical protrusion based on the STM tip model of figure 1(a), leading to the emission of FER electrons from this region. According to field emission theory, electrons at

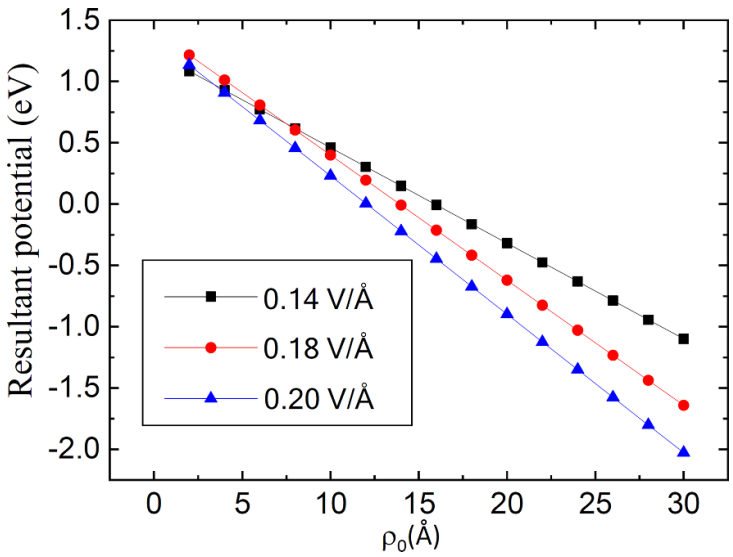

Figure 10. U_r plotted as a function of ρ_0 for three electric fields derived from figure 9(b) at the origin (o) in figure 9(a). Reproduced with permission from [35]. CC BY 3.0.

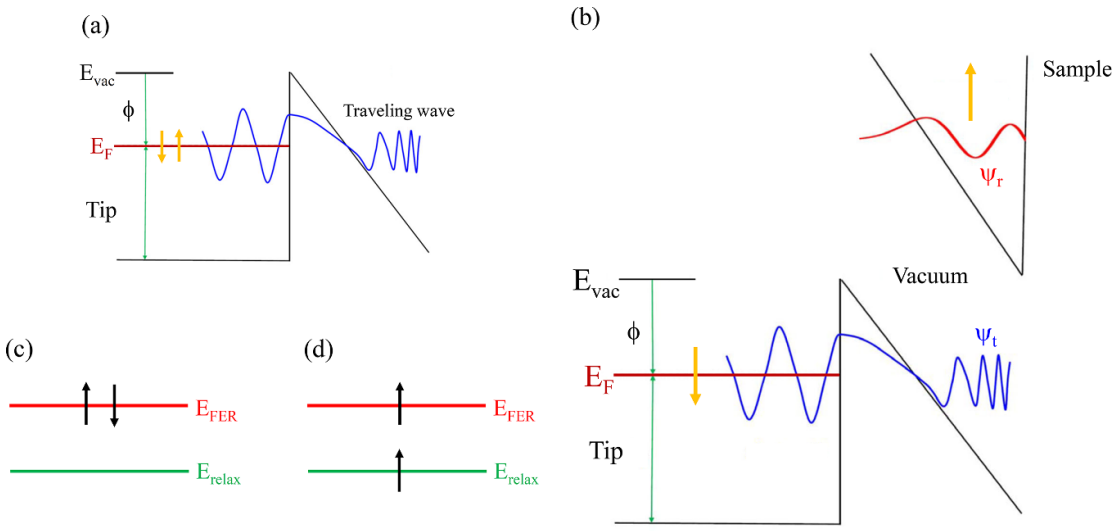

Figure 11. (a) In the field emission state, the vacuum wave function forms a traveling wave, and electrons with opposite spins (marked by arrows) at the energy state where $k_x = 0$, $k_y = 0$, and $k_z = k_F$ (see text) exhibit the highest tunneling probability. (b) In the vacuum, wave function overlap occurs for an FER electron (upper) and an electron in the tip at Fermi level E_F (lower). (c) Exchange interaction enables two electrons with opposite spins to enter the quantized FER state one after the other. (d) Upon relaxation of one resonant electron in (c), its spin flips. Reproduced with permission from [35]. CC BY 3.0.

the tip Fermi level E_F tunnel through the surface energy barrier preferentially, generating the field emission current [figure 11(a)]. This suggests that resonant electrons in FER primarily originate from electrons occupying the energy state at the tip E_F. Since the electric field at the protrusion is strongest in the z direction, the barrier width in this direction is minimal. Consequently, FER electrons are primarily emitted from electrons at the energy state where the lateral wave vector components are zero ($k_x = 0$, $k_y = 0$) and the vertical component equals the Fermi wave vector ($k_z = k_F$) in the tip. This energy state can hold two electrons of opposite spins, as illustrated in figure 11(a). Because the wave function in the vacuum forms a travelling wave, electrons in the tip can tunnel through the energy barrier into the vacuum to cause field emission. Field emission constitutes fundamentally a single-electron tunneling process, implying that electrons are emitted individually.

In the FER, if the spin-up (↑) electron is emitted first, its wave function forms a standing wave ψ_r due to reflection at the surface, as depicted in the upper schematic of figure 11(b). Although the spin-down (↓) electron has not yet been emitted, its travelling wave function ψ_t in the vacuum persists, as shown in the lower schematic. Consequently, the wave functions of these two electrons overlap in the

vacuum, which can induce exchange interaction according to quantum mechanics [61, 62]. As a result, the two electrons are expressed by an antisymmetric total wave function ψ^A, which is expressed either as the product of an antisymmetric total space wave function $\psi_{sp}{}^A$ and a symmetric total spin eigenfunction χ^S [$\psi^A(\uparrow,\downarrow) = \psi_{sp}{}^A(z_\uparrow,z_\downarrow)\cdot\chi^S(\uparrow,\downarrow)$] or as the product of a symmetric total space wave function $\psi_{sp}{}^S$ and an antisymmetric total spin eigenfunction χ^A [$\psi^A(\uparrow,\downarrow) = \psi_{sp}{}^S(z_\uparrow,z_\downarrow)\cdot\chi^A(\uparrow,\downarrow)$]. Here $z_\downarrow$ and $z_\uparrow$ represent the positions of the spin-down and spin-up electrons, respectively. Since the spins are opposite, the total spin eigenfunction is antisymmetric, resulting in a symmetric total space wave function, given by: $\psi_{sp}{}^S = [\psi_r(z_\uparrow)\psi_t(z_\downarrow) + \psi_r(z_\downarrow)\psi_t(z_\uparrow)]/\sqrt{2}$. This symmetry leads to a significantly higher probability density for the two electrons at the same location than for two separated electrons [63]. This outcome suggests that the emission of the spin-up electron can effectively attract the spin-down electron to also emit through the exchange interaction. Therefore, the tunneling process in FER involves the correlated two-electron tunneling, which is fundamentally different from one-electron tunneling in field emission.

3.3.2. Spin flip and Pauli exclusion principle

When two resonant electrons of opposite spins occupy the FER quantized state, one relaxes first by emitting light and flipping its spin, as illustrated in figures 11(c) and (d). Both resonant and relaxed electrons can end up with the same spin. Consequently, the Pauli exclusion principle prevents FER electrons from emitting photons with the relaxed electrons being trapped within the surface potential well. Figure 11(d) illustrates a scenario analogous to the triplet excited state that drives molecular phosphorescence. Therefore, the FER electron's lifetime is determined by how long the relaxed electron continues to be trapped within the well. Figure 9(b) shows that the FER states in each spectrum in figure 3 closely follow the same linear relation, indicating that the F_{FER} for forming these states is identical. Under the same F_{FER}, both the potential well size and the energy of the relaxed electron remain nearly unchanged for all states. As a result, figure 3 demonstrates that all FER peaks exhibits sharp resonances when the well size satisfies the resonance-trapping condition; otherwise, broad resonances are observed.

Figure 6(b) presents two spectra (thin and thick) obtained on Ag(100), selected using the S_2/S_1 versus $1/S_1$ plot, similar to figure 2(a). These spectra demonstrate that the FER energies for orders 1–3 remain nearly identical; however, for orders above 3, a distinct positive energy shift emerges, increasing with order, as shown in the inset. This result indicates that while both spectra were recorded with protrusions of close sharpness, the base radius was larger for the thin spectrum compared to the thick one, akin to the scenario in figure 2(c). Consequently, figure 6(c) reveals that for orders above 3, the FER energy versus $(n - 1/4)^{2/3}$ plot adheres to a linear trend for the thin spectrum, whereas the plot for the thick spectrum deviates from this linearity. Figures 6(d) and (e) further show that the ΔE of FER1 from figure 6(b) can vary by up to fourfold, even at the same F_{FER} (sharpness). This finding indicates that differences in the base radius alter the potential well size, as illustrated in figures 8(d) and (e), thereby influencing the quantum trapping effect.

The absence of a quantum trapping signal in the FER linewidth observed on Ag(111) can be further explained with wave function dissipation (WFD) of resonant electrons under the condition of no energy gap.

4. WFD in FER

Despite the FER wave function being a standing wave, resonant electrons can leave the FER state by transmitting into the surface [31] or by emitting light [59, 60]. Therefore, the wave function is not static but subject to dissipation, a process we term WFD. Prior to exiting the FER state, resonant electrons undergo multiple reflections within the STM junction, completing round trips to maintain the standing wave. WFD leads to a decrease in the probability $\Pr(i)$ that electrons stay in the FER with increasing round-trip number i, with a decay rate $D = \Gamma_l + \Gamma_t$, where Γ_l is the light-emission decay rate per round trip and Γ_t represents the electron transmissivity. $\Pr(i)$ is expressed as:

$$\Pr(i) = (1 - D)^i. \tag{6}$$

Equation (6) indicates that the probability of an electron staying in the FER for i round trips and then leaving on the $(i + 1)$th round trip is $\Pr(i) - \Pr(i + 1)$. For all resonant electrons, the average round-trip number, $\langle i \rangle$, is given by

$$\langle i \rangle = \sum_{i=0}^{i=i_{max}} i[\Pr(i) - \Pr(i+1)], \tag{7}$$

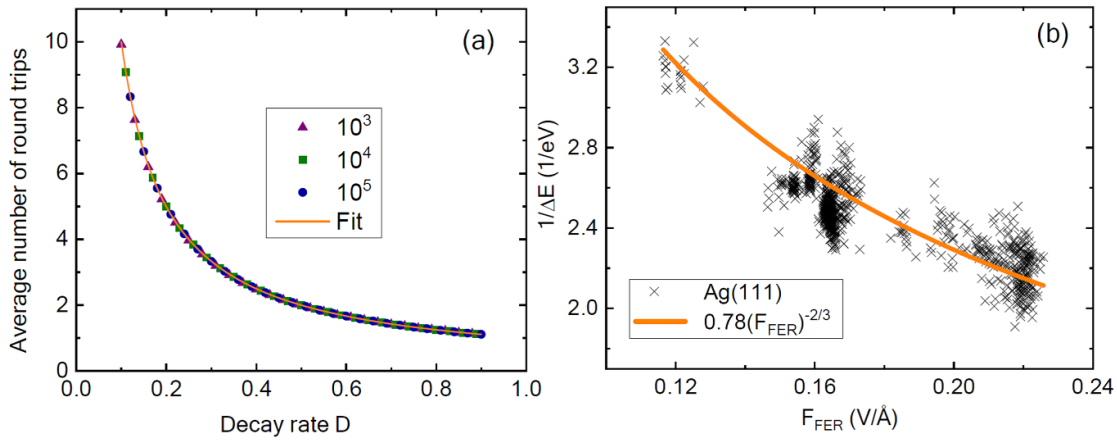

Figure 12. (a) $< i >$ versus D for $N = 10^3$, 10^4, and 10^5, following a trend fitted by a curve $\langle i \rangle = 1/D$. (b) $1/\Delta E$ versus F_{FER} from figure 6(a) for Ag(111), showing that the data points, on average, follow $1/\Delta E \propto F_{\mathrm{FER}}^{-\frac{2}{3}}$. Reprinted (figure) with permission from [36], Copyright (2022) by the American Physical Society.

where $i_{\max}$ represents the maximum round-trip number an electron can complete before exiting the FER state, determined by the total number N of electrons.

Figure 12(a) shows the plot of $< i >$ as a function D, derived from equations (6) and (7) for $N = 10^3$, 10^4, and 10^5. The results indicate that $< i >$ decreases as D increases and is independent of N. This behavior is well described by the relation: $\langle i \rangle = 1/D$. With $N \approx 10^{10}$ in the FER case, the $< i >$ –D plot is expected to reproduce this curve closely.

FER electrons oscillate over a distance s' equal to $(E_{\mathrm{n}} - E_{\mathrm{vac}})/eF_{\mathrm{FER}}$, which spans from the turning point to the surface. The time t of a round trip for a resonant electron is given by $2\ \mathrm{s'} = eF_{\mathrm{FER}}\ \mathrm{t}^2\ \mathrm{m}^{-1}$; together with equations (1) and (2) yields $t = \beta \frac{\left(n-\frac{1}{4}\right)^{\frac{1}{3}}}{F_{\mathrm{FER}}^{\frac{2}{3}}}$, where $\beta = \left(\frac{3\mathrm{m}\hbar\pi}{e^2}\right)^{\frac{1}{3}}$. The average lifetime for electrons in the FER state, which is proportional to $1/\Delta E$, is expressed as $t < \mathrm{i} >$. Thus, D is proportional to ΔE. Because of this relationship, on the Au(111) surface with the reconstruction, FER peaks exhibit an enlarged ΔE in ridge regions, where an enhanced Γ_{t} (and hence higher D) leads to spatial variations in peak intensity [31]. Figure 12(b) presents a plot of $1/\Delta E$ against F_{FER} for Ag(111), according to the results in figure 6(a). Overall, the measurements align with the trend representing $1/\Delta E \propto F_{\mathrm{FER}}^{-\frac{2}{3}}$. Due to $1/\Delta E$ being proportional to $F_{\mathrm{FER}}^{-\frac{2}{3}}/D$, D on Ag(111) remains nearly constant, ignoring slight fluctuation.

According to figure 9(c), the energy of the $n = 4$ FER peak (FER4) in the spectrum with five peaks shown in figure 3(b) lies above the band edge (marked as 3). Although FER4 still presents a sharp peak with $\Delta E = 26.6$ meV, its D is 2.86 times larger than that of FER2, based on the relation $D \propto (n–1/4)^{1/3}\Delta E$. This larger D arises from the inclusion of Γ_{t}, which is equal to 1.86 Γ_{l}, assuming that Γ_{t} for FER2 is 0 due to the presence of the energy gap. Therefore, we suggest that the sharp FER4 peak results from Γ_{l} being smaller than Γ_{t}. In contrast, when Γ_{l} exceeds Γ_{t}, FER4 becomes a broad peak, as observed in the spectrum with six peaks in figure 3(b), where $\Gamma_{\mathrm{t}} = 0.6\ \Gamma_{\mathrm{l}}$, as derived from the ΔE values of FER2 and FER4.

In an invariant potential like the image potential, the round-trip time remains constant. Therefore, for the lifetime of the image-potential state observed by two-photon photoemission [64, 65], the influence of the round-trip time is not evident. In contrast, the potential for the FER state depends on the tip sharpness, causing different round-trip times. The resulting influence on the lifetime arising from the round-trip time becomes observable, as demonstrated in figure 12(b). With $\hbar/\Delta E$ and the measurements in figure 12(b), the lifetime of FER is found to range from 1.26 to 2.19 femtoseconds. Meanwhile, For the same F_{FER} range, the round-trip time is calculated to be 1.73–2.69 femtoseconds. These values indicate that the round-trip time and lifetime are comparable in magnitude.

The energy gap can restrict paired resonant electrons to leave the FER only via light emission, allowing a relaxed electron to coexist with a resonant one. In the absence of an energy gap, the probability of both electrons in a pair emitting light decreases to $\left(\frac{\Gamma_{\mathrm{l}}}{\Gamma_{\mathrm{t}}+\Gamma_{\mathrm{l}}}\right)^2$ due to the competing transmission process. Furthermore, due to the transmission effect, the presence of relaxed electrons in resonance trapping does not substantially extend the resonant-electron lifetimes via the Pauli exclusion principle. Additionally,

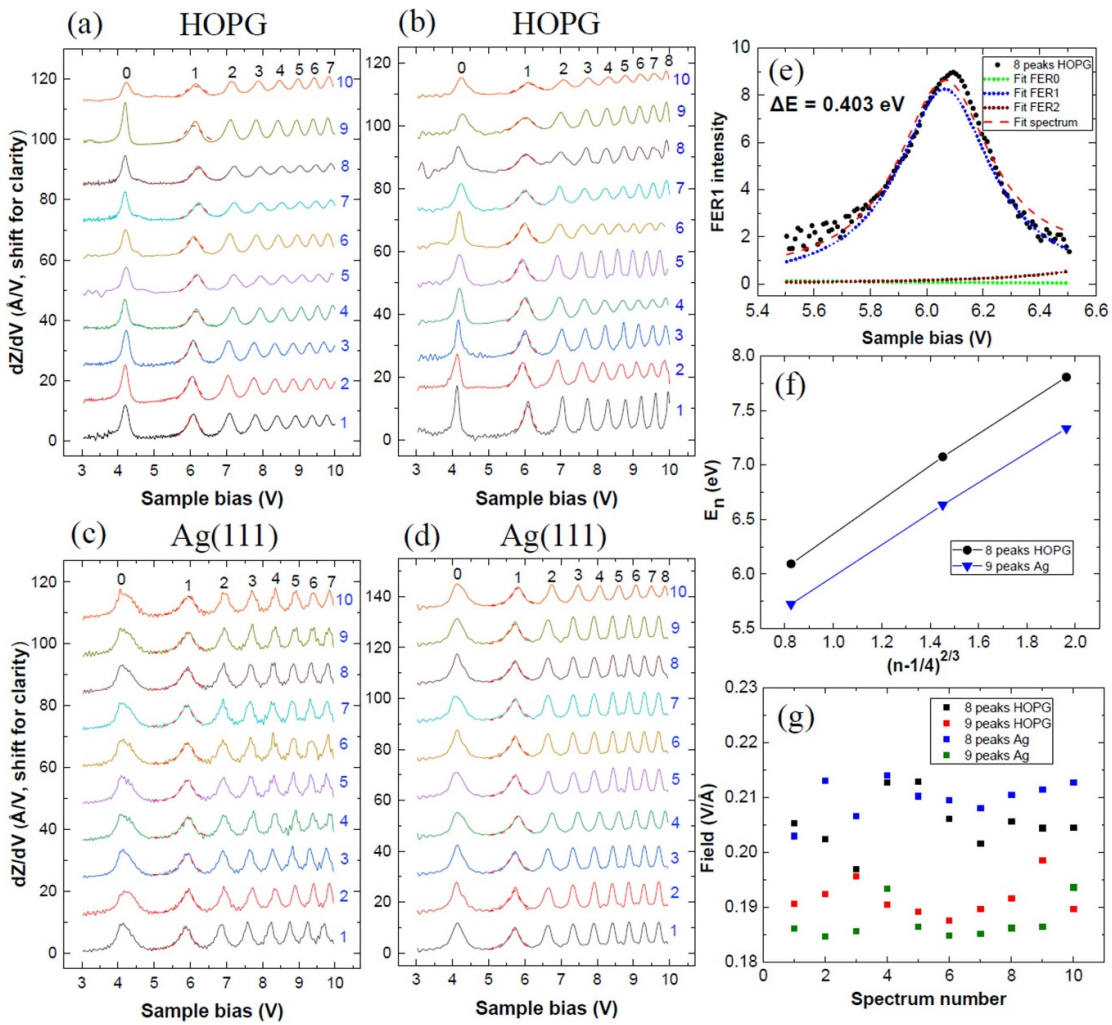

Figure 13. (a) and (b) show FER spectra with eight and nine peaks on HOPG, while (c) and (d) show spectra on Ag(111). Peak orders are labeled above each FER peak. Dashed curves show Lorentzian fits, all in good agreement with FER1. Spectrum numbers on the right are assigned according to FER1 linewidths. (e) Example of ΔE for FER1 obtained from Lorentzian fit on HOPG. (f) Plot of E_n as a function of $(n—1/4)^{2/3}$ for $n = 1$–3, using eight peaks from HOPG and nine from Ag(111), showing linear behavior. The slope yields the F_{FER}. (g) F_{FER} values for FER1 in spectrum from (a)–(d), separating into two groups depending on the FER number. Reproduced from [47]. © The Author(s). Published by IOP Publishing Ltd. CC BY 4.0.

the SDL on Ag(111) may be smaller than that on Ag(100) [47]. These factors result in a weak resonance trapping signal on Ag(111).

Highly oriented pyrolytic graphite (HOPG), as a layered material, differs from metals. This motivated us an investigation into whether WFD on HOPG exhibits behavior distinct from that on Ag(111).

5. Comparison of WFD on HOPG and Ag(111)

5.1. Measuring ΔE and F_{FER}

We investigated WFD on Ag(111) and HOPG surfaces under identical tunneling current and FER number. Repeated Z–V spectroscopy at 30 pA and 78 K on both surfaces was used to obtain the FER spectra. Since the work function of HOPG (4.7 eV) [66] is nearly identical to that of Ag(111) (4.74 eV), an equal FER number signifies comparable STM tip sharpness on the two materials. We therefore selected spectra of matching numbers, as shown in figure 13, presenting FER spectra with eight and nine peaks for HOPG (figures 13(a) and (b), respectively) and for Ag(111) (figures 13(c) and (d)). We focused on ΔE of FER1 in spectra as a case study. The ΔE values were obtained by Lorentzian fitting, as demonstrated for FER1 on HOPG in figure 13(e). The dashed curves in figures 13(a)–(d) denote the Lorentzian fits, revealing excellent agreement with all FER1 peaks. For analysis, the obtained ΔE values of FER1 from spectra with the same peak number were ordered by increasing magnitude and subsequently partitioned into ten sets. From each set, the spectrum exhibiting the largest ΔE was selected for display in figures 13(a)–(d), where the labels on the right indicating the higher ΔE values among the ten sets.

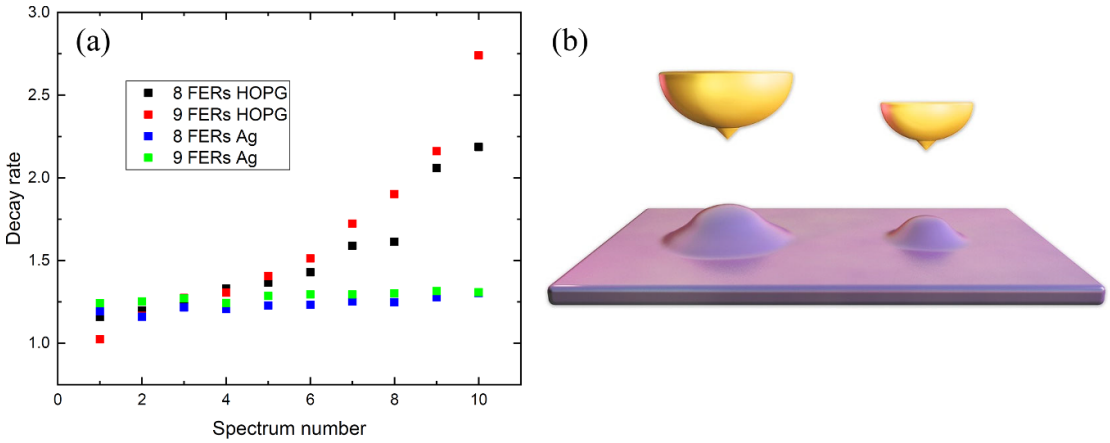

Figure 14. (a) Decay rate of FER1 on Ag(111) and HOPG surfaces as a function of spectrum number for spectra with nine and eight peaks. (b) illustration of dome-shaped deflection on HOPG caused by tips of equal sharpness yet varying base radii, where greater height and diameter indicate a larger deformation level. Reproduced from [47].

Figure 13(f) presents two plots of E_n as a function of $(n - 1/4)^{2/3}$ for $n = 1$–3, corresponding to the spectrum with nine peaks on Ag(111) and eight peaks on HOPG. Both plots reveal linear relationships, indicating that FER energies on HOPG exhibits behavior similar to those on metals, despite HOPG being a layered material. Figure 13(g) shows the F_{FER} values of FER1 in spectra exhibited in figures 13(a)–(d). The results reveal two distinct groups classified by FER number for both Ag(111) and HOPG. The average F_{FER} is higher for FER spectra having eight peaks than for those with nine, while at the same peak number, Ag(111) and HOPG show comparable values.

5.2. The impact of tip-induced attractive deformation (TIAD) on D

For FER1 with $n = 1$, D is given by $(0.75)^{1/3}\Delta E/{F_{FER}}^{2/3}$. Using the values of ΔE and F_{FER}, D was calculated for each FER1 in figure 13. Figure 14(a) plots D for FER1 on HOPG (D_{HOPG}) and Ag(111) (D_{Ag}) as a function of spectrum number N in spectra with eight and nine peaks. While D_{Ag} remained nearly constant across varying N, D_{HOPG} increased rapidly for $N > 5$. We attribute this difference to TIAD, arising from the electrostatic force in the STM junction. The proportional relationship between D and the extent of TIAD will be discussed later. TIAD is greater on HOPG, as the van der Waals interaction between its atomic layers is much weaker than the metallic bond in Ag crystals. This explains why D_{HOPG} exhibited significant variation, whereas D_{Ag} remained stable. Due to the same FER number, the STM tip sharpness levels were comparable on both materials. Thus the variation in D_{HOPG} versus the near constancy of D_{Ag} cannot be attributed to tip sharpness. Instead, we propose that this marked difference arises from variations in the base radius of the tip.

A theoretical study [67] indicates that when the tip-surface distance d falls below the radius R of the base, the electrostatic force F is given by:

$$F = \frac{\pi\varepsilon_0 V_0^2 R}{d}, \tag{8}$$

where V_0 is the bias voltage. A larger R yields a stronger force, resulting in greater deformation of the HOPG surface. Conversely, a smaller base produces weaker deformation (figure 14(b)). TIAD on HOPG takes a dome-like shape, where larger diameter and height correspond to greater deformation. In contrast, Ag crystals are more resistant, so D_{Ag} is less sensitive to changes in R. The electrostatic force was estimated from equation (8) under the assumptions of $d = 2$ nm and $R = 30$ nm for FER1 energy, corresponding to 6 eV. This calculation yields an approximation force of 15 nN.

5.3. WFD under different currents

The TIAD investigated through FER linewidth measurements, as demonstrated earlier, was conducted at a constant current but with different base sizes. Since the force in the STM junction can also be tuned with varying the set current, we further investigated the ΔE values of FER1 for Ag(111) and HOPG under various currents at 5 K. Figure 15(a) shows spectra for HOPG at currents ranging from 0.01 to 1 nA, while figure 15(b) presents spectra for Ag(111) at currents between 0.03 and 10 nA. In both cases,

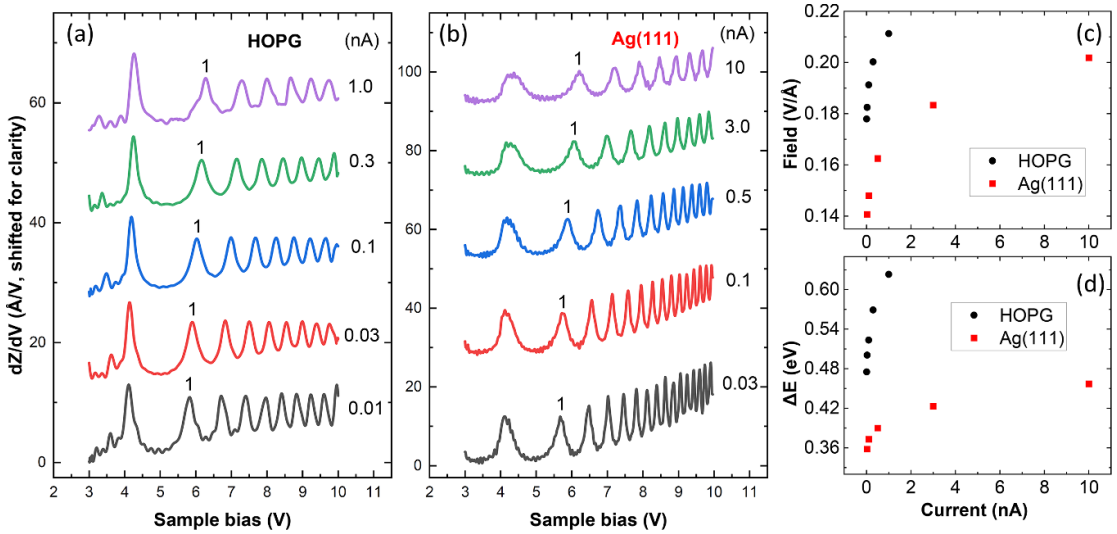

Figure 15. (a) and (b) show FER spectra of the HOPG surface (0.01–1 nA) and the Ag surface (0.03–10 nA), respectively. (c) F_{FER} versus current for HOPG and Ag surfaces. (d) FER1 ΔE versus current for HOPG and Ag surfaces. Reproduced from [47]. © The Author(s). Published by IOP Publishing Ltd. CC BY 4.0.

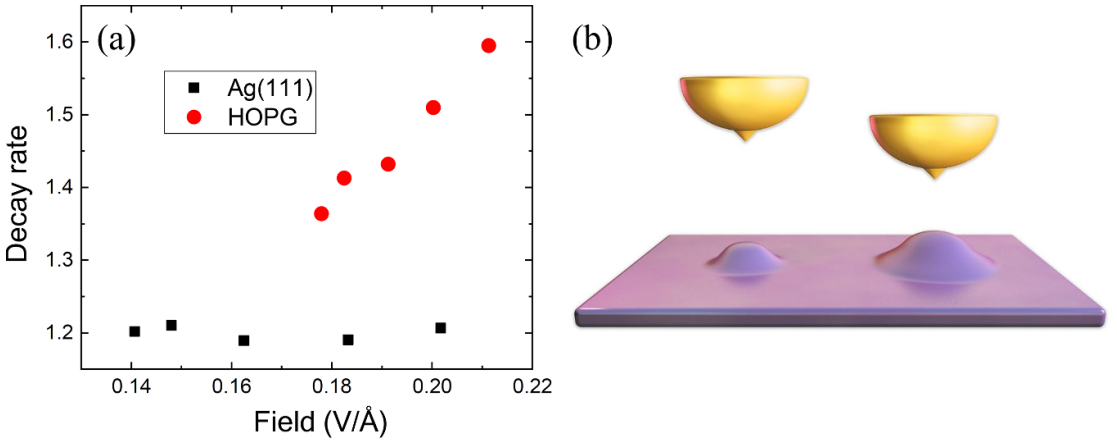

Figure 16. (a) D_{HOPG} increases linearly with F_{FER}, whereas D_{Ag} is insensitive to F_{FER}. (b) TIAD is larger at shorter tip-surface distances and smaller at longer distances. Reproduced from [47]. © The Author(s). Published by IOP Publishing Ltd. CC BY 4.0.

the FER1 peak energy (denoted as '1') shifted to high values with increasing current [68, 69], indicating that F_{FER} increased as the set current rose. Figure 15(c) plots F_{FER} as a function of current, showing smooth trends that indicate stable tip structures on both surfaces for increasing currents. Figure 15(d) reveals that the ΔE values for FER1 increased with the current for both Ag(111) and HOPG. Using the results from figures 15(c) and (d), D_{Ag} and D_{HOPG} versus F_{FER} were calculated, with the results presented in figure 16(a).

Figure 16(a) shows a clear distinction that D_{HOPG} exhibited a linear relationship with F_{FER}, whereas D_{Ag} remained nearly constant. As the force increases with F_{FER}, figure 16(a) highlights that TIAD is substantially more pronounced on HOPG than on Ag(111), in agreement with the findings in figure 14(a). The STM feedback mechanism moves the tip closer to the surface with increasing current. This reduced tip-surface distance amplified the electrostatic force, which in turn attracted and displaced the HOPG surface upward. Consequently, TIAD is larger at shorter tip-surface distances and smaller at longer distances (figure 16(b)).

5.4. DFT calculations

Since Ag(111) and HOPG do not have a band gap, fluctuations in Γ_1 due to quantum trapping effect is minimal. Therefore, in this study, D is considered to depend solely on Γ_t. Because Γ_t varies in proportion to the density of states (DOS) [36], the difference between D_{Ag} and D_{HOPG} can be attributed to variations in the DOS. DFT calculations were used to obtain the DOS values shown in figure 17 for

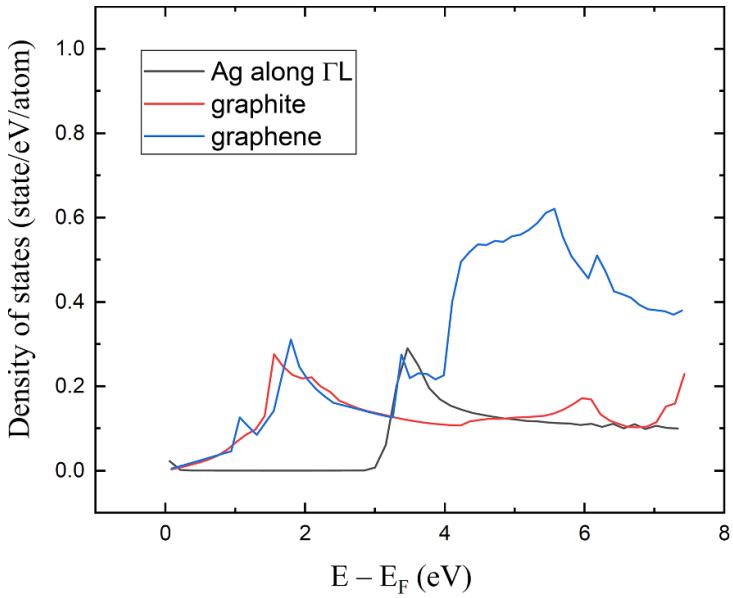

Figure 17. DOS values for Ag(111), HOPG, and single-layer graphene, obtained from DFT calculations. Reproduced from [47]. © The Author(s). Published by IOP Publishing Ltd. CC BY 4.0.

Ag(111), HOPG, and monolayer graphene. At the FER1 energy, approximately 6 eV, the DOS values for Ag(111) and HOPG were comparable, explaining why D_{Ag} and D_{HOPG} are similar for N smaller than 5 in figure 14(a). That is, for HOPG, the base size may be insufficient to induce significant TIAD.

On the other hand, figure 14(a) shows greater variations in D_{HOPG} for $N > 5$, and figure 16(a) reveals that the D_{HOPG} value was linearly proportional to F_{FER}. These two results suggest that DOS grows as TIAD increases. As shown in figure 17, in the vicinity of 6 eV, graphene exhibits higher DOS than HOPG, implying that increasing TIAD gradually shifts the top HOPG layer's electronic structure toward that of graphene, enhancing its DOS.

As a semimetal, HOPG may not fully shield the electric field from penetrating into underlying layers, allowing TIAD to occur there as well. However, the weaker electrostatic force results in a smaller TIAD level than at the top layer. Therefore, the top–subsurface spacing remains larger compared to HOPG without an external field, indicating that the localized electrostatic force separates the top layer to form a quasi-graphene under the STM tip.

6. Summary

This review highlights recent studies demonstrating that the FER linewidth, which reflects the average lifetime of resonant electrons, reveals field-induced effects in the STM junction. These effects include quantum trapping observed on MoS_2 and Ag(100) surfaces and TIAD on HOPG surfaces. Furthermore, on the Ag(111) surface, both effects are nearly undetectable in the FER linewidth, underscoring the role of material properties in their manifestation.

Quantum trapping can induce a significant change in the FER linewidth, up to one order of magnitude, arising from the following mechanisms. (1) Correlated two-electron tunneling: via the exchange interaction, the FER state is filled by two electrons of opposite spins sequentially emitted from the STM tip. (2) One of two electrons emits light with spin flip and turns into a relaxed electron, temporarily trapped within a local potential well due to quantum trapping. (3) With the same spin, the exclusion principle prevents the FER electrons from emitting photons as the relaxed electron stays trapped, thereby substantially extending FER electron lifetimes for the relaxed electrons experiencing resonance trapping.

Because MoS_2 and Ag(100) have a band gap above the vacuum level, which maximizes the two-electron tunneling probability in mechanism (1), most resonant electrons complete the processes described in mechanisms (2) and (3). Conversely, Ag(111) lacks such an energy gap. The resonant electrons can transmit through the surface to significantly reduce the two-electron tunneling probability. As a result, the likelihood of coexistence between resonant and relaxed electrons in mechanisms (2) and (3) is substantially diminished. Additionally, the SDL required to form the potential well on Ag(100) is stronger than on Ag(111). These factors collectively result in a faint quantum trapping signal on Ag(111).

Unlike quantum trapping, the significantly greater TIAD on HOPG compared to Ag(111) is not directly apparent from the FER linewidth. Instead, this TIAD difference, which arises from the much weaker van der Waals force compared to metallic bonding, can be distinguished by analyzing the decay rate of WFD. Under the same FER number and current conditions, the decay rate on HOPG shows significant variation, reflecting different TIAD levels caused by variations in base radii, whereas the decay rate on Ag(111) remains nearly unchanged. Under varying currents, the decay rate on HOPG varies linearly with the electric field, as a stronger electrostatic force leads to higher TIAD levels. In contrast, the decay rate is rather insensitive to the electric field on Ag(111). This linear relationship indicates that the DOS of the top layer of HOPG increases with the electric field. On the other hand, DFT calculations reveal that single-layer graphene exhibits a considerably higher DOS than HOPG at the FER1 energy, indicating that TIAD effectively makes the top layer behave similarly to graphene.

Data availability statement

No new data were created or analysed in this study.

Acknowledgments

The authors appreciate the valuable contributions of S. V. Korachamkandy, H. H. Chang, and W. Y. Chan. This work was supported by Academia Sinica (Grants No: AS-iMATE-111-13 and AS-iMATE-113-13) and the Ministry of Science and Technology (Grant No: NSTC 114-2112-M-001-025), Taiwan.

ORCID iDs

Wei-Bin Su 0000-0002-7555-7634
Horng-Tay Jeng 0000-0002-2881-3826

References

[1] Kleint C 1993 On the early history of field emission including attempts of tunneling spectroscopy *Prog. Surf. Sci.* **42** 101
[2] Gundlach K H 1966 Zur Berechnung Des tunnelstroms durch eine trapezformige potentialstufe *Solid-State Electron.* **9** 949
[3] Lewicki G and Maserjian J 1975 *J. Appl. Phys.* **46** 3032
[4] Binnig G, Rohrer H, Gerber C H and Weibel E 1982 *Phys. Rev. Lett.* **49** 57
[5] Binnig G, Frank K H, Fuchs H, Garcia N, Reihl B, Rohrer H, Salvan F and Williams A R 1985 Tunneling spectroscopy and inverse photoemission—image and field states *Phys. Rev. Lett.* **55** 991
[6] Becker R S, Golovchenko J A and Swartzentruber B S 1985 Electron interferometry at crystal-surfaces *Phys. Rev. Lett.* **55** 987
[7] Bobrov K, Mayne A J and Dujardin G 2001 Atomic-scale imaging of insulating diamond through resonant electron injection *Nature* **413** 616
[8] Liu S, Wolf M and Kumagai T 2018 Plasmon-assisted resonant electron tunneling in a scanning tunneling microscope junction *Phys. Rev. Lett.* **121** 226802
[9] Barimar P S N, Naydenov B, Li J and Boland J J 2017 Spreading resistance at the nano-scale studied by scanning tunneling and field emission spectroscopy *Appl. Phys. Lett.* **110** 263111
[10] Wahl P, Schneider M A, Diekhoner L, Vogelgesang R and Kern K 2003 Quantum coherence of image-potential states *Phys. Rev. Lett.* **91** 106802
[11] Pascual J I, Corriol C, Ceballos G, Aldazabal I, Rust H-P, Horn K, Pitarke J M, Echenique P M and Arnau A 2007 Role of the electric field in surface electron dynamics above the vacuum level *Phys. Rev. B* **75** 165326
[12] Stepanow S, Mugarza A, Ceballos G, Gambardella P, Aldazabal I, Borisov A G and Arnau A 2011 Localization, splitting, and mixing of field emission resonances induced by alkali metal clusters on Cu(100) *Phys. Rev. B* **83** 115101
[13] Craes F, Runte S, Klinkhammer J, Kralj M, Michely T and Busse C 2013 Mapping image potential states on graphene quantum dots *Phys. Rev. Lett.* **111** 056804
[14] Lin C L, Lu S M, Su W B, Shih H T, Wu B F, Yao Y D, Chang C S and Tsong T T 2007 Manifestation of work function difference in high order Gundlach oscillation *Phys. Rev. Lett.* **99** 216103
[15] Huang H-S, Chan W-Y, Su W-B, Hoffmann G and Chang C-S 2013 Measurement of work function difference between Pb/Si(111) and Pb/Ge/Si(111) by high-order Gundlach oscillation *J. Appl. Phys.* **114** 214308
[16] Schulz F, Drost R, Hämäläinen S K, Demonchaux T, Seitsonen A P and Liljeroth P 2014 Epitaxial hexagonal boron nitride on Ir(111): a work function template *Phys. Rev. B* **89** 235429
[17] Gutiérrez C, Brown L, Kim C-J, Park J and Pasupathy A N 2016 Klein tunneling and electron trapping in nanometre-scale graphene quantum dots *Nat. Phys.* **12** 3806
[18] Zhang Q, Yu J, Ebert P, Zhang C, Pan C-R, Chou M-Y, Shih C-K, Zeng C and Yuan S 2018 Tuning Band gap and work function modulations in monolayer hBN/Cu(111) heterostructures with moire patterns *ACS Nano* **12** 9355
[19] Neilson J *et al* 2019 Nitrogen-doped graphene on copper: edge-guided doping process and doping-induced variation of local work function *J. Phys. Chem. C* **123** 8802
[20] Borca B, Castenmiller C, Tsvetanova M, Sotthewes K, Rudenko A N and Zandvliet H J W 2020 Image potential states of germanene *2D Mater.* **7** 035021
[21] Yim C M, Chakraborti D, Rhodes L C, Khim S, Mackenzie A P and Wahl P 2021 Quasiparticle interference and quantum confinement in a correlated Rashba spin-split 2D electron liquid *Sci. Adv.* **7** eabd7361

[22] Kumar A, Banerjee K, Ervasti M M, Kezilebieke S, Dvorak M, Rinke P, Harju A and Liljeroth P 2021 Electronic characterization of a charge-transfer complex monolayer on graphene *ACS Nano* **15** 9945
[23] Carnevali V, Sala A, Biasin P, Panighel M, Comelli G, Peressi M and Africh C 2023 Probing the graphene/substrate interaction by electron tunneling decay *Carbon* **210** 118055
[24] Girard Y, Benbouabdellah S, Chahib O, Chacon C, Bellec A, Repain V, Lagoute J, Dappe Y J, González C and Su W-B 2023 Growth and local electronic properties of Cobalt nanodots underneath graphene on SiC(0001) *Carbon* **208** 22
[25] Yue C G, Huang Z Q, Wang W-L, Gao Z A, Lin H C, Liu J W and Chang K 2024 Identification and manipulation of atomic defects in monolayer SnSe *ACS Nano* **18** 25478
[26] Wojciechowski P, Andrzejewska W, Dobrotvorska M V, Wang Y, Milosz Z, Ossowski T and Lewandowski M 2024 Structure of monolayer iron nitride islands on Cu(001) revisited *Vacuum* **220** 112716
[27] Wu Q L, Quan W Z, Pan S Y, Hu J Y, Zhang Z H, Wang J, Zheng F P and Zhang Y F 2024 Atomically thin kagome-structured Co_9Te_{16} achieved through self-intercalation and its flat band visualization *Nano Lett.* **24** 7672
[28] Borca B and Zandvliet H J W 2024 Image potential states of 2D materials *Appl. Mater. Today* **39** 102304
[29] Sagisaka K and Fujita D 2008 Unusual mosaic image of the Si(111)-(7×7) surface coinciding with field emission resonance in scanning tunneling microscopy *Phys. Rev. B* **77** 205301
[30] Rienks E D L, Nilius N, Rust H-P and Freund H-J 2005 Surface potential of a polar oxide film: feO on Pt(111) *Phys. Rev. B* **71** 241404
[31] Su W B, Lu S M, Lin C L, Shih H T, Jiang C L, Chang C S and Tsong T T 2007 Interplay between transmission background and Gundlach oscillation in scanning tunneling spectroscopy *Phys. Rev. B* **75** 195406
[32] Chan W-Y, Lu S-M, Su W-B, Liao C-C, Hoffmann G, Tsai T-R and Chang C-S 2017 Sharpness-induced energy shifts of quantum well states in Pb islands on Cu(111) *Nanotechnology* **28** 095706
[33] Lu S-M, Chan W-Y, Su W-B, Pai W W, Liu H-L and Chang C-S 2018 Characterization of external potential for field emission resonances and its applications on nanometer-scale measurements *New J. Phys.* **20** 043014
[34] Su W-B, Lin C-L, Chan W-Y, Lu S-M and Chang C-S 2016 Field enhancement factors and self-focus functions manifesting in field emission resonances in scanning tunneling microscopy *Nanotechnology* **27** 175705
[35] Su W-B, Lu S-M, Jeng H-T, Chan W-Y, Chang H-H, Pai W W, Liu H-L and Chang C-S 2020 Observing quantum trapping on MoS_2 through the lifetimes of resonant electrons: revealing the Pauli exclusion principle *Nanoscale Adv.* **2** 5848
[36] Su W-B, Lu S-M, Chang H-H, Jeng H-T, Chan W-Y, Jiang P-C, Lin K-H and Chang C-S 2022 Impact of band structure on wave function dissipation in field emission resonance *Phys. Rev. B* **105** 195411
[37] Altfeder I B, Narayanamurti V and Chen D M 2002 *Phys. Rev. Lett.* **88** 206801
[38] Su W B, Chang S H, Jian W B, Chang C S, Chen L J and Tsong T T 2001 *Phys. Rev. Lett.* **86** 5116
[39] Chung W F, Feng Y J, Poon H C, Chan C T, Tong S Y and Altman M S 2003 *Phys. Rev. Lett.* **90** 216105
[40] Su W B, Lu S M, Shih H T, Jiang C L, Chang C S and Tsong T T 2006 *J. Phys.: Condens. Matter* **18** 6299
[41] Limot L, Maroutian T, Johansson P and Berndt R 2003 Surface-state stark shift in a scanning tunneling microscope *Phys. Rev. Lett.* **91** 196801
[42] Ogawa S, Heike S, Takahashi H and Hashizume T 2007 Tip-induced energy shift in Au/Fe(100) quantum wells *Phys. Rev. B* **75** 115319
[43] Su W B, Lu S M, Jiang C L, Shih H T, Chang C S and Tsong T T 2006 Stark shift of transmission resonance in scanning tunneling spectroscopy *Phys. Rev. B* **74** 155330
[44] Chan W Y, Huang H S, Su W B, Lin W H, Jeng H-T, Wu M K and Chang C S 2012 Field-induced expansion deformation in Pb islands on Cu(111): evidence from energy shift of empty quantum-well states *Phys. Rev. Lett.* **108** 146102
[45] Breitwieser R, Hu Y-C, Chao Y C, Li R-J, Tzeng Y R, Li L-J, Liou S-C, Lin K C, Chen C W and Pai W W 2014 Flipping nanoscale ripples of free-standing graphene using a scanning tunneling microscope tip *Carbon* **77** 236
[46] Weng S-W, Lin W-H, Su W-B, Hwu E-T, Chen P L, Tsai T-R and Chang C-S 2014 Estimating Young's modulus of graphene with Raman scattering enhanced by micrometer tip *Nanotechnology* **25** 255703
[47] Korachamkandy S V, Lu S-M, Su W-B, Chan W-Y, Chang H-H, Jeng H-T, Lee C-H and Chang C-S 2022 Probing tip-induced attractive deformation of graphite surfaces through wave function dissipation in field emission resonance *J. Phys. Commun.* **6** 075010
[48] Korachamkandy S V, Lu S-M, Chan W-Y, Chang H-H, Lee C-H and Su W-B 2022 Characterization of apex structures of scanning tunneling microscope tips with field emission resonance energies *Jpn. J. Appl. Phys.* **61** 085001
[49] Nayfeh M H and Brussel M K 1985 *Electricity and Magnetism* (Wiley) pp 49
[50] Lang N D and Kohn W 1970 *Phys. Rev. B* **1** 4555
[51] Lu C-P, Li G, Watanabe K, Taniguchi T and Andrei E Y 2014 MoS2: choice substrate for accessing and tuning the electronic properties of grapheme *Phys. Rev. Lett.* **113** 156804
[52] Feenstra R M, Dong Y, Semtsiv M P and Masselink W T 2016 Influence of tip-induced band bending on tunneling spectra of semiconductor surfaces *Nanotechnol* **18** 044015
[53] Kresse G and Furthmuller J 1996 Efficiency of *ab−initio* total energy calculations for metals and semiconductors using a plane−wave basis set *Comput. Mater. Sci.* **6** 15
[54] Kresse G 1995 *Ab initio* molecular dynamics for liquid metals *J. Non-Cryst. Solids* **192–193** 222
[55] Kresse G and Furthmuller J 1996 Efficient iterative schemes for *ab initio* total−energy calculations using a plane−wave basis set *Phys. Rev. B* **54** 11169
[56] Perdew J P, Chevary J A, Vosko S H, Jackson K A, Pederson M R, Singh D J and Fiolhais C 1992 Atoms, molecules, solids, and surfaces: applications of the generalized gradient approximation for exchange and correlation *Phys. Rev. B* **46** 6671
[57] Perdew J P and Wang Y 1992 Pair−distribution function and its coupling−constant average for the spin−polarized electron−gas *Phys. Rev. B* **46** 12947
[58] Popov I, Seifert G and Tomanek D 2012 Designing electrical contacts to MoS2 monolayers: a computational study *Phys. Rev. Lett.* **108** 156802
[59] Coombs J, Gimzewski J, Reihl B, Sass J and Schlittler R 1988 Photon emission experiments with the scanning tunneling microscope *J. Microsc.* **152** 325
[60] Martínez-Blanco J and Fölsch S 2015 *J. Phys.: Condens. Matter* **27** 255008
[61] Heisenberg W 1926 Mehrkörperproblem und Resonanz in der Quantenmechanik *Z. Physik.* **38** 411
[62] Dirac P A M 1926 On the theory of quantum mechanics *Proc. R. Soc. A* **112** 661
[63] Eisberg R and Resnick R 1985 *Quantum Physics of Atoms, Molecules, Solids, Nuclei, and Particles* 2nd edn Wiley p 314

[64] Schuppler S, Fischer N, Fauster T and Steinmann W 1992 *Phys. Rev. B* **46** 13539
[65] Berthold W, Höfer U, Feulner P, Chulkov E V, Silkin V M and Echenique P M 2002 *Phys. Rev. Lett.* **88** 056805
[66] Rut'kov E V, Afanas'eva E Y and Gall N R 2020 Graphene and graphite work function depending on layer number on Re *Diam. Relat. Mater.* **101** 107576
[67] Belaidi S, Girard P and Leveque G 1997 Electrostatic forces acting on the tip in atomic force microscopy: modelization and comparison with analytic expressions *J. Appl. Phys.* **81** 1023
[68] Dougherty D, Maksymovych P, Lee J, Feng M, Petek H and Yates J Jr 2007 *Phys. Rev. B* **76** 125428
[69] Su W-B, Chan W-Y, Lu S-M, Chang H-H and Chang C-S 2024 Tip-induced local Fermi level alignment: a Stark shift in vacuum level in scanning tunneling microscope configurations *Chin. J. Phys.* **92** 877